Available online at www.sciencedirect.com

ScienceDirect

International Journal of Heat and Mass Transfer 50 (2007) 872–880

International Journal of HEAT and MASS TRANSFER

www.elsevier.com/locate/ijhmt

Three-dimensional thermocapillary–buoyancy flow of silicone oil in a differentially heated annular pool

Lan Peng [a], You-Rong Li [a,*], Wan-Yuan Shi [a,b], Nobuyuki Imaishi [b]

[a] *College of Power Engineering, Chongqing University, Chongqing 400044, China*
[b] *Institute for Materials Chemistry and Engineering, Kyushu University, Fukuoka, Japan*

Received 17 November 2005; received in revised form 21 August 2006
Available online 23 October 2006

Abstract

In order to understand the characteristics of thermocapillary–buoyancy flow, we conducted a series of unsteady three-dimensional numerical simulations of thermocapillary–buoyancy flow of 0.65cSt silicone oil (Prandtl number $Pr = 6.7$) in an annular pool with different depth ($d = 1$–11 mm) heated from the outer wall (radius $r_o = 40$ mm) and cooled at the inner cylinder ($r_i = 20$ mm) with an adiabatic solid bottom and adiabatic free surface. Simulation conditions correspond to those in the experiments of Schwabe [D. Schwabe, Buoyant–thermocapillary and pure thermocapillary convective instabilities in Czochralski systems, J. Crystal Growth 237–239 (2002) 1849–1853]. Simulation results with large Marangoni number predict three types three-dimensional flow patterns. In the shallow thin pool ($d = 1$ mm), the hydrothermal wave characterized by curved spokes is dominant. In the deep pools ($d \geqslant 5$ mm) the three-dimensional stationary flow appears and this flow pattern corresponds to the Rayleigh-Benard instability, which consists of pairs of counter-rotating longitudinal rolls. When $2\ \text{mm} \leqslant d \leqslant 4$ mm, the hydrothermal wave and three-dimensional oscillatory flow coexist in the pool and travel along the same azimuthal direction with the same angular velocity. The critical conditions for the onset of three-dimensional flows were determined and compared with the experimental results. The characteristics of three-dimensional flows were discussed.

Keywords: Thermocapillary–buoyancy flow; Hydrothermal wave; Silicone oil; Annular pool; Numerical simulation

---

1. Introduction

The dynamic behavior of flows driven by a horizontal temperature gradient in fluid layers with a free upper surface has attracted the attention of the researchers for many years. More recently, thermocapillary–buoyancy convection becomes very important in both fundamental and industrial aspects. It is well-known that the coupled thermocapillary–buoyancy convection in the crucible is very complex and influences the homogeneity and quality of the grown crystal directly during the Czochralski (CZ) growth technique of the crystal. Smith and Davis [1] first achieved the linear stability analysis in an infinitely extended thin fluid layer with a free upper surface subjected to a constant horizontal temperature gradient in the absence of gravity forces. To verify the influence of buoyancy forces, Laure and Roux [2] conducted much research for the low Prandtl number (Pr) fluids and Parmentier et al. [3] for liquids with Pr up to 10.

At the same time, many experiments of pure thermocapillary or thermocapillary–buoyancy convection were carried out for liquid pools in rectangular geometries [4–12], annular geometries [13–16] and open cylindrical containers [17,18]. The results of these experiments would help the understanding to various types of flow instabilities. Burguete et al. [12] found that thermocapillary–buoyancy convection could destabilize into different patterns, depending on the temperature difference ΔT and liquid pool depth d. For small d values, the system exhibits the hydrothermal waves (HTW) while for larger d values, the stationary

---

[*] Corresponding author. Tel.: +86 23 6511 2284; fax: +86 23 6510 2473.
E-mail address: liyourong@cqu.edu.cn (Y.-R. Li).

0017-9310/$ - see front matter © 2006 Elsevier Ltd. All rights reserved.
doi:10.1016/j.ijheatmasstransfer.2006.08.015

Nomenclature

Bo_d	dynamic Bond number, Eq. (9)
d	depth, m
$\boldsymbol{e}_z$	z-directional unit vector
g	gravitational acceleration, $g = 9.806$ m s^{-2}
Gr	Grashoff number, Eq. (10)
m	azimuthal wave number
Ma	Marangoni number, Eq. (11)
p	pressure, Pa
P	nondimensional pressure
Pr	Prandtl number, Eq. (12)
r	radius, m
R	nondimensional radius
Ra	Rayleigh number, Eq. (13)
t	time, s
T	temperature, K
v	velocity, m s^{-1}
V	nondimensional velocity
$\boldsymbol{V}$	nondimensional velocity vector
z	axial coordinate, m
Z	nondimensional axial coordinate

Greek symbols

α	thermal diffusivity, m^2 s^{-1}
β	growth rate constant
γ_T	temperature coefficient of surface tension, N m^{-1} K^{-1}
θ	azimuthal coordinate, rad
μ	dynamic viscosity, kg m^{-1} s^{-1}
ν	kinematic viscosity, m^2 s^{-1}
ρ	density, kg m^{-3}
ρ_T	thermal expansion coefficient, K^{-1}
ψ	nondimensional stream function

Subscripts

c	cold or counter
cri	critical
h	hotter
i	inner
o	outer
r, R	radial
z, Z	axial
θ	azimuthal

longitudinal rolls (SR) are observed. Garnier et al. [15] observed HTW with spiral-like arms in thin annular pools of silicone oil between an inner cold rod with 8 mm of diameter and an outer wall with 135 mm of diameter, and with depth 1.2 mm or 1.9 mm. They also found a pulsating target-like wave patterns (i.e., coaxial circles traveling outward in the radial direction) dominant only near the cold inner wall as well as the curves arms of HTW in the whole area of the liquid surface. Kamotani et al. [17,18] conducted a large set of microgravity experiments of oscillatory thermocapillary flow in open cylindrical containers of silicone oil with the depth 1.2, 2.0 and 3.0 cm, in which the liquid was heated from its center. They observed two or three lobed patterns. Recently, Schwabe et al. [19–22] reported convection experiments with silicone oil in a Czochralski model system and annular pool at normal gravity and under microgravity. In their experiments, the annular gaps of 0.65cSt silicone oil with an outer heated wall of radius $r_o = 40$ mm, an inner cooled cylinder of $r_i = 20$ mm, and with a liquid depth adjustable in the range of $d = 2.5$–20 mm, were subjected to various radial temperature gradients. They observed thermocapillary flow penetrates fully into the fluid volume under microgravity whereas it is a separated surface tension driven convection roll at the free surface under normal gravity. They also determined the onset conditions of the oscillations and found that gravity significantly stabilizes the basic steady radial thermocapillary flow of silicone oil, in an annular pool heated from the outer wall, by comparing their results of on-ground experiments and microgravity experiment on FOTON-12 satellite. They confirmed that the three-dimensional stationary instability (3DSI) consisted of pairs of counter-rotating longitudinal rolls and found it existed at the liquid depth as low as 3 mm. The wavelength of this 3DSI has been observed near its onset for the first time and the limits for the onset of the 3DSI are estimated from a corresponding linear extrapolation of the velocity amplitudes and temperature amplitudes.

Obviously, it is rather difficult to observe the details of the various flow patterns through the experiments. The recent development of the computers allows us to conduct large scales three-dimensional (3D) unsteady numerical simulations. Xu and Zebib [23] conducted the numerical simulation of HTW in a rectangular pool and obtained a stability diagram and wave numbers. Bucchignani [24] numerically simulated HTW in a rectangular cavity of silicone oil ($Pr = 13.9$) at $\Delta T = 372$ K under zero gravity. The wavelength and propagation angle are similar to those predicted by the linear stability analysis of Smith and Davis and also the experiments of Riley and Neitzel [10]. Thermocapillary flow of silicone oil was worked out by Sim et al. [25] in open annulus with the same geometry as that of Schwabe's experiment on FOTON-12. Li et al. [26,27] showed the traveling waves and its stability diagram in an annular pool to compare with microgravity experiments of Schwabe et al. They found that the wave patterns varied with pool depth. In very shallow liquid layers ($d = 1.0$–1.5 mm), HTW with curved spokes is dominant. While in deeper pools, straight spokes appear and move slowly in the azimuthal direction. Up to now, there is a lack of numerical simulations of 3D thermocapillary–buoyancy flows. In the present study, we extended our previous work [27] so as to evaluate the effect of buoyancy forces on the flow instability and compare with the experimental results of Schwabe [22] in annular pools of moderate-Prandtl-number fluid.

2. Model formulation

2.1. Basic assumptions and governing equations

We analyze thermocapillary–buoyancy flow of the 0.65cSt silicone oil ($Pr = 6.7$) in an annular pool of depth d, inner radius r_i and outer radius r_o, with a free upper surface and a solid bottom, as shown schematically in Fig. 1. The inner and outer cylinders are maintained at the constant temperature T_c and T_h ($T_h > T_c$), respectively. The following is assumed in our model: (1) Silicone oil is an incompressible Newtonian fluid and the Boussinesq approximation is applicable except for the surface tension. (2) The velocity is low and the flow is laminar. (3) The upper surface is flat and nondeformable. (4) At the free surface, the thermocapillary force is taken into account. At other solid-liquid boundaries, the no-slip condition is applied. (5) Both bottom and top boundaries are assumed to be adiabatic.

With the above assumptions, the flow and heat transfer equations are expressed in a nondimensional form as follows:

$$\nabla \cdot \boldsymbol{V} = 0, \tag{1}$$

$$\frac{\partial \boldsymbol{V}}{\partial \tau} + \boldsymbol{V} \cdot \nabla \boldsymbol{V} = -\nabla P + \nabla^2 \boldsymbol{V} + Gr\Theta \boldsymbol{e}_z, \tag{2}$$

$$\frac{\partial \Theta}{\partial \tau} + \boldsymbol{V} \cdot \nabla \Theta = \frac{1}{Pr}\nabla^2 \Theta. \tag{3}$$

The boundary conditions at the free surface ($Z = d/r_o$, $R_i < R < 1$, $0 \leqslant \theta < 2\pi$)

$$\frac{\partial V_R}{\partial Z} = \frac{Ma}{Pr}\frac{\partial \Theta}{\partial R}, \quad \frac{\partial V_\theta}{\partial Z} = \frac{Ma}{Pr}\frac{\partial \Theta}{R\partial \theta}, \quad V_Z = 0, \tag{4a–c}$$

$$\frac{\partial \Theta}{\partial Z} = 0, \tag{4d}$$

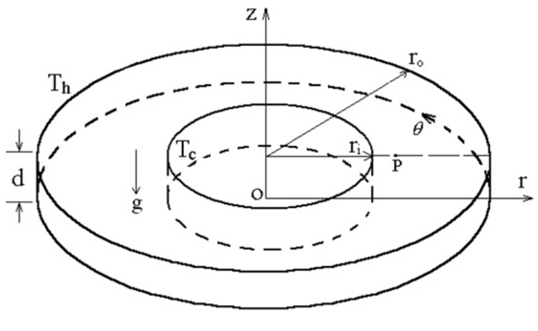

Fig. 1. Configuration of model system.

at the bottom ($Z = 0$, $R_i < R < 1$, $0 \leqslant \theta < 2\pi$)

$$V_R = V_\theta = V_Z = 0, \tag{5a–c}$$

$$\frac{\partial \Theta}{\partial Z} = 0, \tag{5d}$$

at the inner cylinder ($R = R_i$, $0 \leqslant Z \leqslant d/r_o$, $0 \leqslant \theta < 2\pi$)

$$V_R = V_\theta = V_Z = 0, \tag{6a–c}$$

$$\Theta = \Theta_i = 0, \tag{6d}$$

and at the outer cylinder ($R = 1$, $0 \leqslant Z \leqslant d/r_o$, $0 \leqslant \theta < 2\pi$)

$$V_R = V_\theta = V_Z = 0, \tag{7a–c}$$

$$\Theta = \Theta_o = 1. \tag{7d}$$

The initial conditions are expressed as follows (at $\tau = 0$):

$$V_R = V_\theta = V_Z = 0, \quad \Theta = 1 - \ln R/\ln R_i. \tag{8a–d}$$

The variables are nondimensionalized as

$$(R, Z) = \frac{(r, z)}{r_o}, \quad (V_R, V_\theta, V_Z) = \frac{(v_r, v_\theta, v_z)}{\nu/r_o}, \quad P = \frac{pr_o^2}{\rho \nu^2},$$
$$\Theta = \frac{T - T_c}{T_h - T_c}, \quad \tau = \frac{t\nu}{r_o^2}.$$

The dimensionless parameters are defined as follows:

$$\text{Dynamic bond number:} \quad Bo_d = \frac{\rho g \rho_T d^2}{\gamma_T}, \tag{9}$$

$$\text{Grashoff number:} \quad Gr = \frac{\rho_T g \Delta T r_o^3}{\nu^2}, \tag{10}$$

$$\text{Marangoni number:} \quad Ma = \frac{\gamma_T(\partial T/\partial r)d^2}{\mu\alpha} \approx \frac{\gamma_T d^2}{\mu\alpha}\frac{\Delta T}{r_o - r_i}, \tag{11}$$

$$\text{Prandtl number:} \quad Pr = \frac{\nu}{\alpha}, \tag{12}$$

$$\text{Rayleigh number:} \quad Ra = Ma \cdot Bo_d = \frac{g\rho_T(\partial T/\partial r)d^4}{\nu\alpha}, \tag{13}$$

where $\Delta T = T_h - T_c$. The geometric parameters used in this work are chosen to simulate the experiments of Schwabe [22]. The depth of the annular pool is $d = (1–11)$ mm. The thermophysical properties of the 0.65cSt silicone oil at 20 °C are listed in Table 1.

2.2. Numerical method

The fundamental equations were discretized by the control volume method. The central difference approximation

Table 1
Physical properties of the 0.65cSt silicone oil

Symbol	Value	Unit
α	0.97×10^{-7}	$m^2\,s^{-1}$
ν	0.65×10^{-6}	$m^2\,s^{-1}$
ρ	760	$kg\,m^{-3}$
γ_T	-8.0×10^{-5}	$N\,m^{-1}\,K^{-1}$
ρ_T	1.34×10^{-3}	K^{-1}
Pr	6.7	–

Table 2
Mesh dependence for $d = 1$ mm, $Ma = 667.8$ ($\Delta T = 8$ K) and $Bo_d = 0.125$

Mesh	Frequency (Hz)	Wave number
$82^R \times 16^Z \times 123^\theta$	2D stable flow	–
$102^R \times 16^Z \times 163^\theta$	0.6585	22
$102^R \times 16^Z \times 203^\theta$	0.6686	24
$102^R \times 16^Z \times 243^\theta$	0.6721	24

was applied to the diffusion terms while the second-order upwind scheme was used for the convective terms. The discretized equations were solved by a full implicit method in time marching. The SIMPLEC algorithm [28] was used to handle the pressure coupling. To solve the Poisson equation, the preconditioned Bi-CGSTAB algorithm [29] was applied.

Numerical simulations were conducted on an MPU of Fujitsu VPP700 at the Computer Center of Kyushu University. The nondimensional time increment between 10^{-6} and 4×10^{-6} was chosen, which corresponds approximately to $(2 \sim 8) \times 10^{-3}$ s. Convergence at each time step was assumed if the maximum nondimensional residual error of the continuity equation among all control volumes became less than 10^{-8}.

In this study, nonuniform staggered grids of $102^r \times (16–36)^z \times 243^\theta$ were used. To check the grid convergence, the simulations with four different meshes were performed for $d = 1$ mm and $Ma = 667.8$ ($\Delta T = 8$ K). These grids produced the similar surface spoke patterns and space-time characteristics. However, the wave number m and frequency f of temperature oscillation at the monitoring point $P(R = 0.625,\ \theta = 0)$ on the free surface showed the small grid dependence, as shown in Table 2. Therefore, the meshes selected in this study were sufficient for the accurate simulation. For other depths, sufficient grid convergence was confirmed for each mesh. The validation of the code for the thermocapillary and thermocapillary–buoyancy flow simulation was performed in our previous works [26,27,30–32], and will not be repeated here.

3. Results and discussion

Any radial temperature difference produces a surface tension gradient on the free surface, and the Marangoni effect and the buoyancy force induce the flow in the fluid layer. In the present case, the surface fluid flows from the outer cylinder toward the inner cylinder and the recirculation flow exists in the fluid volume. If the temperature gradient is small, a steady axisymmetric flow develops in the fluid layer. This type of flow is called as the “basic flow”. However, with the temperature gradient increasing, this basic flow becomes unstable against 3D disturbances in shallow pools ($d \leqslant 4$ mm) and the three-dimensional stationary flow (3DSF) in deep pools ($d \geqslant 5$ mm). In the following sections, the critical conditions for this flow transition and the characteristics for the nonlinear 3D oscillatory flow and 3DSF are precisely examined by the numerical simulations.

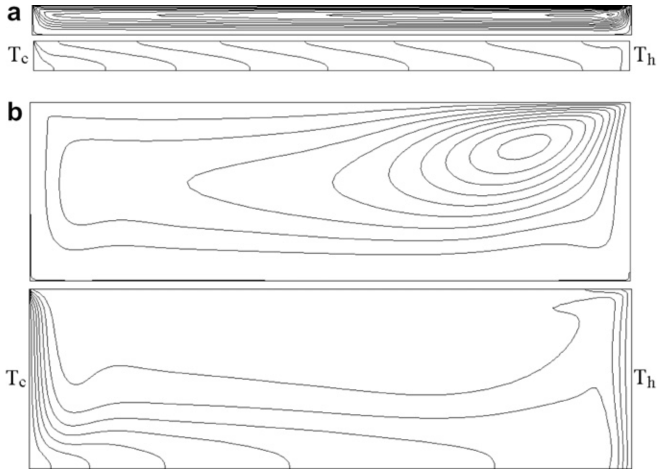

Fig. 2. Streamlines and isotherms of the basic flow. (a) $d = 1$ mm, $Ma = 167$ ($\Delta T = 2$ K), $Bo_d = 0.125$, $\psi_{max} = 0.62$, $\delta\psi = 0.06$, $\delta\theta = 0.1$; (b) $d = 6$ mm, $Ma = 6010$ ($\Delta T = 2$ K), $Bo_d = 4.5$, $\psi_{max} = 4.70$, $\delta\psi = 0.50$, $\delta\theta = 0.1$.

3.1. Basic flow

A set of typical streamlines and isotherms of the basic steady flow is shown in Fig. 2. Transient time to establish these steady basic flow fields ranges between $\tau = 0.02$ and 0.08. The basic flow is characterized by its single roll cell structure with the rapid surface flow inward from the hot outer wall to the cold inner wall and an outward return flow near the bottom. But, a second corotating roll cell appears in thin fluid layers ($d \leqslant 3$ mm). The strength of the second co-rotating cell is enhanced as the temperature difference increases. Because of the low thermal conductivity of the fluid, the thermal boundary layers appear near the inner and outer walls. As Ma (ΔT) increases, the temperature drop in these boundary layers raises and eventually the surface temperature gradient in the mid-surface decreases. Therefore, the radial velocity decreases due to the decrease in the radial temperature gradient in the mid-region of the surface. It should be noted that there appeared a strong roll cell near the hot wall driven by the large surface temperature drop there. In contrast, a very large temperature drop near the cold inner wall causes a steep increase in surface velocity, followed by a steep deceleration down to zero at the cold wall. This sharp velocity peak appears only on the surface. No such large velocity peak appears in the bulk fluid near the cold wall.

3.2. Critical condition for flow transition

For the shallow pools ($d \leqslant 4$ mm), when Ma (ΔT) exceeds a certain threshold value, 3D disturbances are incubated and the amplitudes of the azimuthal velocity V_θ at the monitoring point P ($R = 0.625$, $\theta = 0$) on the free surface increase with time. Finally, a 3D oscillatory flow pattern is formed. The present numerical simulations with

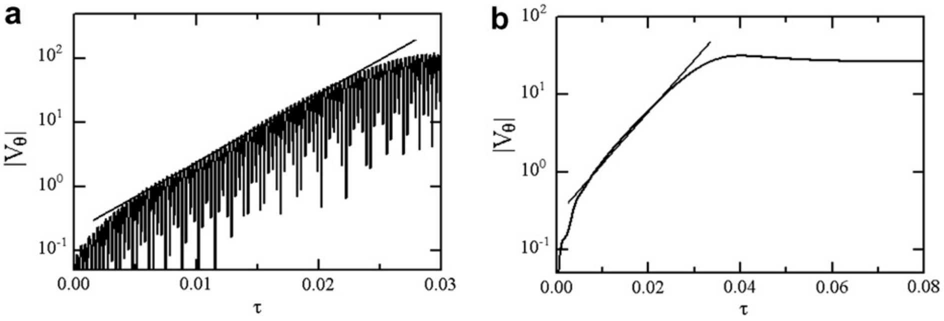

Fig. 3. Growth of the azimuthal velocity at monitoring point P. (a) $d = 1$ mm, $Ma = 835$ ($\Delta T = 10$ K), $Bo_d = 0.125$; (b) $d = 6$ mm, $Ma = 18031$ ($\Delta T = 6$ K), $Bo_d = 4.5$.

large Ma (ΔT) show that during the initial growth process the intensity of any disturbance (X) can be expressed by

$$X(R,\theta,Z,\tau) = X_0(R,\theta,Z,0)\exp[(\beta + i\beta_1)\tau], \tag{14}$$

where β is the growth rate constant of the disturbance and β_I represents the time-dependent oscillatory characteristics of the disturbance. The typical example of growth of the azimuthal velocity at monitoring point P is shown in Fig. 3(a). The β-value can be determined from the slope of the semi-logarithmic plot of $V_{\theta,\max}$ vs. τ. By plotting β vs. Ma (ΔT), we can determine the critical Ma (ΔT), which is defined as the neutral stability limit ($\beta = 0$) [27].

For the deep pools ($d \geqslant 5$ mm), when Ma (ΔT) exceeds a certain threshold value, 3D disturbances start an exponential growth and finally a 3DSF field is established. The mode and growth process of the 3D disturbance are characterized by the azimuthal wave number m and the growth rate constant β. The growth of any 3D disturbance (X) can be expressed approximately by

$$X(R,\theta,Z,\tau) \approx X_0(R,\theta,Z,0)\sin(2\pi m\theta)\exp(\beta\tau). \tag{15}$$

The typical example of growth of the azimuthal velocity at the monitoring point P is shown in Fig. 3(b). We can also determine the critical Ma (ΔT).

Fig. 4 shows the present results of the critical Ma (ΔT) compared with the experimental results obtained by Schwabe [22]. The critical values obtained in the present simulation show a good agreement with the experimental ones.

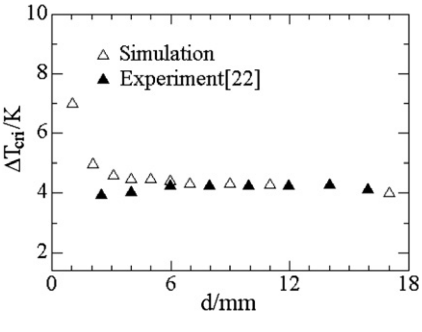

Fig. 4. Comparison of the simulation results and the experimental results of the critical values.

3.3. Hydrothermal waves

Fig. 5(a) and (b) shows the characteristics of the 3D oscillatory flow in a very thin annular pool of $d = 1$ mm, including the snapshots of surface temperature fluctuation distribution and the space-time diagram (STD) of surface

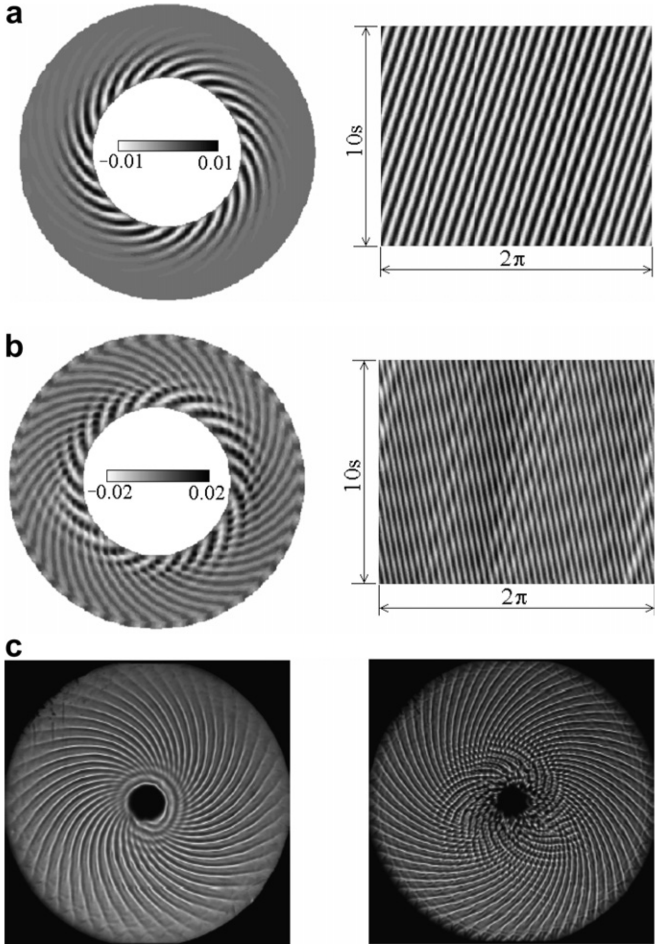

Fig. 5. Snapshots of surface temperature fluctuation and space–time diagram of surface temperature distribution at $R = 0.625$. (a) $d = 1$ mm, $Ma = 667.8$ ($\Delta T = 8$ K), $Bo_d = 0.125$; (b) $d = 1$ mm, $Ma = 1002$ ($\Delta T = 12$ K), $Bo_d = 0.125$; (c) Experimental results [15], left: $d = 1.9$ mm, $\Delta T = 14.25$ K, right: $d = 1.2$ mm, $\Delta T = 20$ K.

temperature distribution along a circumference at $R = 0.625$. Fluctuation (δX) of a physical quantity X is introduced to extract the 3D disturbances

$$\delta X(R,\theta,Z,\tau) = X(R,\theta,Z,\tau) - \frac{1}{2\pi}\int_0^{2\pi} X(R,\theta,Z,\tau)\mathrm{d}\theta. \quad (16)$$

From Fig. 5, we found that many traveling curved spoke patterns prevail on the entire surface area. These traveling patterns correspond to the "hydrothermal wave" instability. Under a small Ma (ΔT) number, for example, $Ma = 667.8$ ($\Delta T = 8$ K), the hydrothermal waves propagate in the counterclockwise direction, as shown in Fig. 5(a). The angle (ϕ) between the wave propagation and the negative direction of temperature gradient, measured at $R = 0.625$, is about 155°–160°, which is close to those predicted by the linear stability theory for the infinite rectangular layer for $Pr = 10$ [1] and an experimental result (0.83π) obtained in a rectangular pool of silicone oil ($Pr = 10.3$) [12]. These traveling waves are indicated as the many parallel slanted straight lines on the STD. In cases with a small Ma, the HTW patterns are clearly observable only in the inner part of the pool, being faded in the outer region. As Ma increases, HTWs become dominant over the whole area of the liquid surface. The azimuthal wave number m will decrease from 24 to 21 when the temperature difference rises from 7 K to 10 K. But, the oscillation frequency f will increase, as shown in Fig. 6.

Simulation with a larger Ma (ΔT), such as $Ma = 1002$ ($\Delta T = 12$ K), indicates two groups of HTW coexisting in the pool with the different wave numbers and the different traveling directions, as shown in Fig. 5(b). Interferences between two groups of HTW occur throughout almost the entire volume of the pool. Typical values of the wave number are $m = 22$ (counterclockwise direction) and $m = 44$ (clockwise direction). The coexistence of two groups of HTW is also reported by Garnier et al. [15], as shown in Fig. 5(c), although his pool geometry is different from that of the present system. However, we do not observe "target-like (coaxial) waves" ($m = 0$) propagating outward in the radial direction, which were reported by Garnier et al. near the inner wall of his annular pool which had much larger outer wall and smaller inner wall radiuses. The larger inner wall radius in the present system can produce a surface temperature gradient near the inner wall that is less than the critical value, which is necessary for the incipience of the target-like waves.

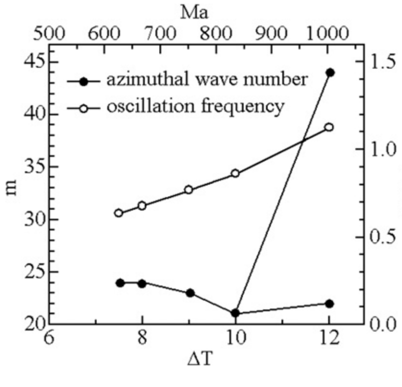

Fig. 6. Variation of wave number m and oscillation frequency f at monitoring point P as functions of $Ma(\Delta T)$.

3.4. Three-dimensional stationary flow

For the deep layers of $d \geqslant 5$ mm, the simulation results are different from those of $d = 1$ mm. Fig. 7 shows the snapshot of surface temperature fluctuation distribution and the STD of surface temperature along a circumference at $R = 0.625$ for the layer of $d = 6$ mm at $Ma = 30051$ ($\Delta T = 10$ K). In this case, many straight spoke patterns are observed over the entire surface area, but they do not move. As a result, STD is indicated as the many vertical lines. The number m of the spoke patterns is about 16 and independent on the Ma number and the pool depth d. This flow pattern belongs to the 3DSF. The mechanism is explained as follows.

The Marangoni effect generates an inward radial flow (hereafter we denote this as the Ma-driven flow) near the free surface. Therefore, the temperature at the free surface is always higher than that at the bottom. Because the radial temperature drops are mainly concentrated in the vertical thermal boundary layers near the inner and outer walls, the flow driven by the buoyancy force (the B-driven flow) near the hotter wall carries the low temperature liquid to the area below the free surface, as shown in Fig. 8(a). At the same time, the return flow carries high temperature liquid on the free surface to the area below the B-driven flow. Therefore, there exists a region with the counter temperature gradient layer near the hotter wall; its depth is d_c, as shown in Fig. 8(b). In the counter temperature gradient layer, Rayleigh-Benard instability is produced and extended to the free surface when the Ra number exceeds a certain threshold value. As shown in Fig. 8(c), it suggests that the 3DSF consists of pairs of counter-rotating longitudinal rolls (whose axes are oriented parallel to the applied horizontal temperature gradient) that are superimposed on the basic flow, and this result has a good agreement with the experiment of Schwabe [19]. In order to prove that

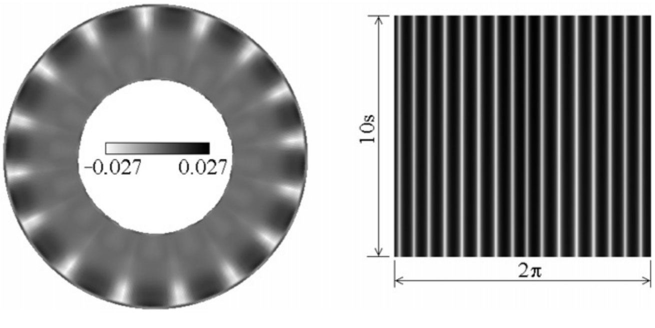

Fig. 7. Snapshots of surface temperature fluctuation and space–time diagram of surface temperature distribution at $R = 0.625$ for the 3DSF. $d = 6$ mm, $Ma = 30051$ ($\Delta T = 10$ K), $Bo_d = 4.5$.

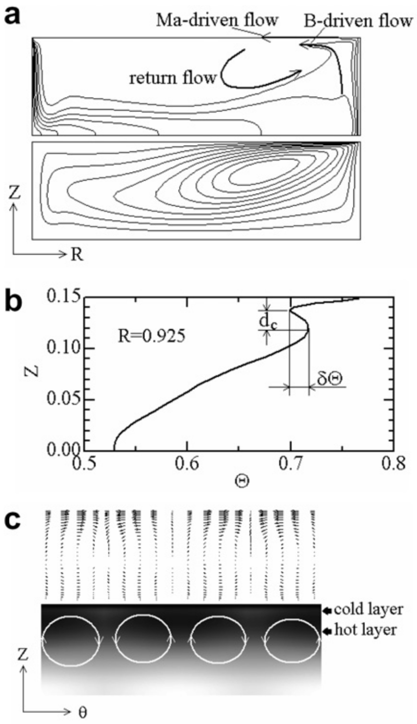

Fig. 8. The mechanism of the 3DSF. $d = 6$ mm, $Ma = 30051$ ($\Delta T = 10$ K), $Bo_d = 4.5$. (a) Isotherms and pseudo-streamlines at the plane of $\theta = 0$. (b) Temperature as a function of Z at $\theta = 0$. (c) Counter-rotating longitudinal rolls at $R = 0.925$ at the plane of Z–θ.

the 3DSF corresponds to the Rayleigh-Benard instability, the local Ra number is estimated. When $d = 6$ mm and $Ma = 18030$ ($\Delta T = 6$ K), the maximum depth d_c of the counter temperature gradient layer is found to be about 2.32 mm and the maximum vertical temperature difference δT_c is estimated to be 0.28 K from the simulated results. In this case, the local Rayleigh number defined as $Ra = g\rho_T \delta T d_c^3/(\nu\alpha)$, is about 728. It implies that the local Ra number would exceed the critical Ra number value, $Ra_{cri} = 657.5$, which was obtained by the linear stability analysis [33] for the incipience of the Rayleigh-Benard instability in an infinitely extended fluid layer with the free upper and nether surfaces subjected to a constant vertical temperature gradient. Therefore, we speculate that the 3DSF is the result of the Rayleigh-Benard instability within the counter temperature gradient layer. It should be noted that there appeared an isothermal zone on the upper pool near the inner wall, where the temperature oscillatory was very small.

3.5. Combined hydrothermal waves and 3D oscillatory flow

When 2 mm $\leqslant d \leqslant$ 4 mm, combined hydrothermal waves and 3D oscillatory flow (3DOF) appear on the free surface, as shown in Fig. 9(a). In this case, the vertical temperature gradient near the inner wall is large enough to form the "hydrothermal wave" instability. Therefore, the HTW patterns are clearly observable in the inner part of the pool. But, the counter temperature gradient layer near the hotter wall also exists, as shown in Fig. 9(b). Accordingly, pairs of counter-rotating longitudinal rolls are dominant in this region. These rolls will propagate in the azimuthal direction driven by HTW, which causes axes of rolls that are not parallel to the temperature gradient. In this case, the wave number of the 3DOF is the same as that of HTW.

Fig. 10 shows the different regimes for the buoyancy–thermocapillary flow, depending on the dynamical Bond number Bo_d (the fluid depth d). In a shallow pool, for example $d = 1$ mm, the Bo_d ($=Ra/Ma$) number is about 0.125, and the thermocapillary force is dominant. The hydrothermal wave characterized by curved spokes appears on the free surface. While in the deep pools of $d \geqslant 5$ mm, $Bo_d \geqslant 3.12$, the buoyancy force is dominant. The 3DSF appears due to the Rayleigh-Benard instability. When $0.5 \leqslant Bo_d \leqslant 2$ (2 mm $\leqslant d \leqslant$ 4 mm), the HTW and

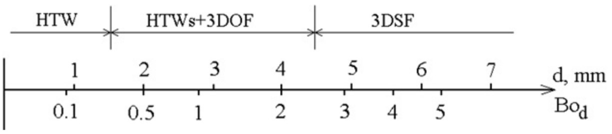

Fig. 10. Different regimes for the thermocapillary–buoyancy flow, depending on the dynamical Bond number Bo_d (the fluid depth d).

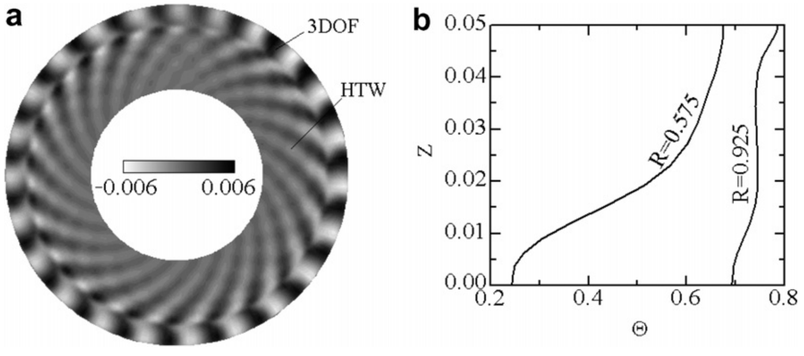

Fig. 9. Combined hydrothermal waves and 3D oscillatory flow at $d = 2$ mm, $Ma = 3339$ ($\Delta T = 10$ K) and $Bo_d = 0.5$. (a) Snapshots of surface temperature fluctuation. (b) Temperature as a function of Z at $\theta = 0$.

the 3DOF coexist in the pool and travel in the same azimuthal direction with the same angular velocity.

4. Conclusions

A series of 3D numerical simulations of the thermocapillary–buoyancy flows in annular pools of silicone oil ($Pr = 6.7$) were conducted by means of the finite volume method. From the simulation results, the following conclusions were obtained.

(1) In a shallow thin pool ($d = 1$ mm), the hydrothermal wave characterized by the curved spokes is dominant. Under small Ma number, there is only one group of HTW. The azimuthal wave number m decrease and oscillation frequency f increases as Ma increases. Under larger Ma number, two groups of HTW with different wave numbers and different traveling directions coexist in the pool.
(2) When $2 \leqslant d \leqslant 4$ mm, HTW and 3DOF coexist in the pool and travel in the same azimuthal direction with the same angular velocity. In this case, the wave number of the 3DOF is the same as that of HTW.
(3) In the deep pools ($d \geqslant 5$ mm) the 3DSF appears. This flow pattern corresponds to the Rayleigh-Benard instability, which consists of pairs of counter-rotating longitudinal rolls. The number m of the spoke patterns is about 16 and independent on the Ma number and the pool depth d.
(4) The critical conditions for the onset of the 3D flows are determined and show a good agreement with the corresponding experimental data [22].
(5) The numerical results in the deep pools give the qualitative explanation of the experimental results of the 3DSF.

Acknowledgements

This work is supported by National Natural Science Foundation of China (Grant No. 50476042) and the Scientific Research Foundation for the Returned Overseas Chinese Scholars, State Education Ministry (Grant No. 2005-383).

References

[1] M.K. Smith, S.H. Davis, Instabilities of dynamic thermocapillary liquid layers. Part 1. Convective instabilities, J. Fluid Mech. 132 (1983) 119–144.
[2] P. Laure, B. Roux, Linear and non-linear analysis of the Hadley circulation, J. Crystal Growth 97 (1989) 226–234.
[3] P.M. Parmentier, V.C. Reynier, G. Lebon, Buoyant–thermocapillary instabilities in medium Prandtl number fluid layers subject to a horizontal temperature gradient, Int. J. Heat Mass Transfer 36 (1993) 2417–2427.
[4] D. Villers, J.K. Platten, Coupled buoyancy and Marangoni convection in acetone: experiments and comparison with numerical simulations, J. Fluid Mech. 234 (1992) 487–510.
[5] F. Daviaud, J.M. Vince, Traveling waves in a fluid layer subjected to a horizontal temperature gradient, Phys. Rev. E 48 (1993) 4432–4436.
[6] M.G. Braunsfurth, G.M. Homsy, Combined thermocapillary–buoyancy convection in a cavity. Part II. An experimental study, Phys. Fluids 9 (1997) 1277–1286.
[7] A. Garcimartin, N. Mukolobwiez, F. Daviaud, Origin of waves in surface-tension-driven convection, Phys. Rev. E 56 (1997) 1699–1705.
[8] R.J. Riley, G.P. Neitzel, Instability of thermocapillary–buoyancy convection in shallow layers. Part 1. Characterization of steady and oscillatory instabilities, J. Fluid Mech. 359 (1998) 143–164.
[9] S. Benz, P. Hintz, R.J. Riley, G.P. Neitzel, Instability of thermocapillary–buoyancy convection in shallow layers. Part 2. Suppression of hydrothermal waves, J. Fluid Mech. 359 (1998) 165–180.
[10] M.A. Pelacho, J. Burguete, Temperature oscillations of hydrothermal waves in thermocapillary–buoyancy convection, Phys. Rev. E 59 (1999) 835–840.
[11] M.A. Pelacho, A. Garcimartin, J. Burguete, Local Marangoni number at the onset of hydrothermal waves, Phys. Rev. E 62 (2000) 477–483.
[12] J. Burguete, N. Mukolobwiez, F. Daviaud, N. Garnier, A. Chiffaudel, Buoyant–thermocapillary instabilities in extended liquid layers subjected to a horizontal temperature gradient, Phys. Fluids 13 (2001) 2773–2787.
[13] A.B. Ezersky, A. Garcimartin, J. Burguete, H.L. Mancini, C. Perez-Garcia, Hydrothermal waves in Marangoni convection in a cylindrical container, Phys. Rev. E 47 (1993) 1126–1131.
[14] N. Mukolobwiez, A. Chiffaudel, F. Daviaud, Supercritical Eckhaus instability for surface-tension-driven hydrothermal waves, Phys. Rev. Lett. 80 (1998) 4661–4664.
[15] N. Garnier, A. Chiffaudel, Two dimensional hydrothermal waves in an extended cylindrical vessel, Eur. Phys. J. B 19 (2001) 87–95.
[16] T. Azami, S. Nakamura, M. Eguchi, T. Hibiya, The role of surface-tension-driven flow in the formation of a surface pattern on a Czochralski silicon melt, J. Crystal Growth 233 (2001) 99–107.
[17] Y. Kamotani, Thermocapillary flow under microgravity – experimental results, Adv. Space Res. 24 (1999) 1357–1366.
[18] Y. Kamotani, S. Ostrach, J. Masud, Microgravity experiments and analysis of oscillatory thermocapillary flow in cylindrical containers, J. Fluid Mech. 410 (2000) 211–233.
[19] S. Benz, D. Schwabe, The three-dimensional stationary instability in dynamic thermocapillary shallow cavities, Exp. Fluids 31 (2001) 409–416.
[20] D. Schwabe, S. Benz, Thermocapillary flow instabilities in an annulus under microgravity – results of the experiment MAGIA, Adv. Space Res. 29 (2002) 629–638.
[21] P. Hintz, D. Schwabe, H. Wilke, Convection in a Czochralski crucible – Part 1: non-rotating crystal, J. Crystal Growth 222 (2001) 343–355.
[22] D. Schwabe, Buoyant–thermocapillary and pure thermocapillary convective instabilities in Czochralski systems, J. Crystal Growth 237-239 (2002) 1849–1853.
[23] J. Xu, A. Zebib, Oscillatory two- and three-dimensional thermocapillary convection, J. Fluid Mech. 364 (1998) 187–209.
[24] E. Bucchignani, Numerical Characterization of Hydrothermal Waves in a Laterally Heated Shallow Layer, Phys. Fluids 16 (2004) 3839–3849.
[25] B.C. Sim, A. Zebib, D. Schwabe, Oscillatory thermocapillary convection in open cylindrical annuli. Part 2. simulations, J. Fluid Mech. 491 (2003) 259–274.
[26] Y.R. Li, L. Peng, S.Y. Wu, D.L. Zeng, N. Imaishi, Thermocapillary convection in a differentially heated annular pool for moderate Prandtl number fluid, Int. J. Thermal Sci. 43 (2004) 587–593.
[27] Y.R. Li, L. Peng, Y. Akiyama, N. Imaishi, Three-dimensional numerical simulation of thermocapillary flow of moderate prandtl number fluid in an annular pool, J. Crystal Growth 259 (2003) 374–387.
[28] S.V. Patanker, Numerical Heat Transfer and Fluid Flow (Series in Comput. Math. in Mechanics and Thermal Sciences), McGraw-Hill, New York, 1980.

[29] H.A. Van Der Vorst, Bi-CGSTAB: a fast and smoothly converging variant of Bi-CG for the solution of nonsymmetric linear systems, SIAM J. Sci. Stat. Comput. 13 (1992) 631–644.
[30] Y.R. Li, N. Imaishi, T. Azami, T. Hibiya, Three-dimensional oscillatory flow in a thin annular pool of silicon melt, J. Crystal Growth 260 (2004) 28–42.
[31] Y.R. Li, X.J. Quan, L. Peng, N. Imaishi, S.Y. Wu, D.L. Zeng, Three-dimensional thermocapillary-buoyancy flow in a shallow molten silicon pool with Cz configuration, Int. J. Heat Mass Transfer 48 (2005) 952–1960.
[32] Y.R. Li, Y.J. Liu, L. Peng, Y. Wang, Three-dimensional oscillatory thermocapillary flow in encapsulated liquid bridge, Phys. Fluids 18 (2006) 074108.
[33] D.L. Zeng, Engineering Nonequilibrium Thermodynamics, Science China Press, Beijing, 1991.